Eur. Phys. J. D **21**, 271–283 (2002)
DOI: 10.1140/epjd/e2002-00208-x

THE EUROPEAN PHYSICAL JOURNAL D

Collisional deexcitation of exotic hydrogen atoms in highly excited states

II. Cascade calculations

T.S. Jensen[1,2,a] and V.E. Markushin[1]

[1] Paul Scherrer Institute, 5232 Villigen PSI, Switzerland
[2] Institut für Theoretische Physik der Universität Zürich, Winterthurerstrasse 190, 8057 Zürich, Switzerland

Received 28 May 2002
Published online 15 October 2002 – © EDP Sciences, Società Italiana di Fisica, Springer-Verlag 2002

Abstract. The atomic cascades in $\mu^- p$ and $\bar{p}p$ atoms have been studied in detail using new results for the cross-sections of the scattering of highly excited exotic atoms from molecular hydrogen. The cascade calculations have been done with an updated version of the extended standard cascade model that computes the evolution in the kinetic energy from the beginning of the cascade. The resulting X-ray yields, kinetic energy distributions, and cascade times are compared with the experimental data.

PACS. 36.10.-k Exotic atoms and molecules (containing mesons, muons, and other unusual particles)

1 Introduction

The standard cascade model (SCM) of exotic hydrogen atoms, originally introduced by Leon and Bethe [1] and later extended to include the evolution of the kinetic energy distribution during the atomic cascade [2,3], provides a fair description of many properties of atomic cascades, such as the X-ray yields and absorption fractions [4–7]. However, no detailed calculations of the initial stage of the cascade were done until recently due to the lack of the corresponding cross-sections. The upper stage of the cascade was commonly described with a phenomenological deexcitation mechanism, the so-called chemical deexcitation [1]. This mechanism was introduced in order to explain the data on cascade times, as the external Auger effect was found to be too slow at the initial stage of the cascade. The exact nature of the collisional deexcitation of highly excited exotic atoms remained a mystery for a long time until experimental studies of the initial stages of the atomic cascade became possible. Recently the energy distributions of $\pi^- p$, $\mu^- p$, and $\mu^- d$ atoms were studied with various time-of-flight methods [8–12]. In particular, the measurements performed with $\mu^- p$ and $\bar{p}p$ at low density allow one to probe collisional deexcitation mechanisms for highly excited states as long as the energy distribution remains frozen during the lower cascade stage dominated by the radiative transitions.

In our recent paper [13], we studied the dynamics of collisional deexcitation of highly excited exotic atoms using the classical-trajectory Monte Carlo method. The Coulomb transitions with large change of principal quantum number n were found to be the dominant collisional deexcitation mechanism at high n, with the molecular structure of the hydrogen target being essential for the dominance of transitions with large Δn. The main goal of this paper is to investigate the atomic cascades in hydrogen-like atoms at low density and to confront the theoretical results with the experimental data on the X-ray yields, cascade times, and kinetic energy distributions for muonic and antiprotonic hydrogen. As the lower part of the atomic cascade at low target densities is mainly dominated by the radiative deexcitation, the results of our calculations are only weakly affected by theoretical uncertainties in the collisional cross-sections for the low n states. The detailed cascade calculations for high density targets will be published elsewhere.

The article is organized as follows. The cascade model is described in Section 2. The results of the cascade calculations for the $\mu^- p$ and $\bar{p}p$ atoms are presented in Section 3. The conclusions are summarized in Section 4.

2 The extended standard cascade model

2.1 Overview

The extended standard cascade model (ESCM) is a kinetics model that includes all cascade processes of the standard cascade model [1,4,7]: the radiative, Auger, and Coulomb deexcitation, Stark mixing, and, in case of hadronic atoms, nuclear absorption (see Tab. 1 and references therein). In addition, the ESCM also takes into

[a] e-mail: thomas@physik.unizh.ch

Table 1. Processes included in the extended standard cascade model.

Process	Example	References
Stark mixing	$(x^-p)_{nl_i} + \mathrm{H}_2 \rightarrow (x^-p)_{nl_\mathrm{f}} + \mathrm{H}_2^*$	[13,16–18]
External Auger effect	$(x^-p)_i + \mathrm{H} \rightarrow (x^-p)_\mathrm{f} + p + e^-$	[13,19]
Coulomb deexcitation	$(x^-p)_{n_i} + \mathrm{H}_2 \rightarrow (x^-p)_{n_\mathrm{f}} + \mathrm{H}_2^*,\ n_\mathrm{f} < n_i$	[13,18]
Elastic	$(x^-p)_{nl} + \mathrm{H}_2 \rightarrow (x^-p)_{nl} + \mathrm{H}_2^*$	[13,16]
Absorption	$(\pi^-p)_i + \mathrm{H} \rightarrow \pi^0 + n + \mathrm{H}$	[16–18]
Radiative	$(x^-p)_{n_il_i} \rightarrow (x^-p)_{n_\mathrm{f}l_\mathrm{f}} + \gamma$	[20]
Nuclear reaction	$(\pi^-p)_{ns} \rightarrow \pi^0 + n,\ \gamma + n$	[1]
Weak decay	$\pi^- \rightarrow \mu^-\bar{\nu}_\mu$	

account the interaction between internal and external degrees of freedom of the exotic atom: the kinetic energy distribution changes during the cascade due to the acceleration and deceleration mechanisms [2,3,14,15]. The new results for the collisional processes presented in [13,16] are used in the present version of the ESCM, a significant improvement over the previous calculations.

The cascade in exotic atoms is divided into two parts: the classical domain for high n and the quantum mechanical domain for low n. The x^-p can be described classically for quantum numbers $n \gg 1$, and for convenience we use the properties of the Auger deexcitation to define the n-ranges of the two domains. The Auger deexcitation rates are known to have a maximum for $n = n_\mathrm{c}$ where n_c is the largest n for which the binding energy released in a $\Delta n = 1$ transition is enough to ionize the H_2 molecule [1,13,19]: $n_\mathrm{c} = 7$ for μ^-p and $n_\mathrm{c} = 12$ for $\bar{p}p$. Our calculations show that the Coulomb deexcitation dominates the Auger deexcitation for $n > n_\mathrm{c}$ [13]. We define the classical domain by the conditions $n > n_\mathrm{c}$. The classical domain, where the processes were calculated in the classical Monte Carlo (CMC) model with the molecular structure of the target taken into account, will be discussed in Section 2.2. In the quantum mechanical domain, $n \leq n_\mathrm{c}$, the close-coupling method and semiclassical approximations [16,17,21] were used to calculate the differential cross-sections, $\mathrm{d}\sigma/\mathrm{d}\cos\theta$, of the collisional processes

$$(x^-p)_{nl} + \mathrm{H} \rightarrow (x^-p)_{nl'} + \mathrm{H} \tag{1}$$

and the cross-sections for absorption during collision and Auger transitions

$$(x^-p)_{nl} + \mathrm{H} \rightarrow \text{absorption}, \tag{2}$$

$$(x^-p)_{n_il_i} + \mathrm{H} \rightarrow (x^-p)_{n_\mathrm{f}} + p + e^- \tag{3}$$

in an energy range relevant for atomic cascade. The new calculations allow us to describe the competition between deceleration and Stark mixing, as well as the absorption in hadronic atoms due to Stark collisions, without employing any fitting parameters related to the Stark mixing and deceleration, like k_Stk used in many earlier calculations [4]. Our cascade code makes full use of the differential cross-sections so that the kinetics is treated more accurately than in cascade models using continuous deceleration [22].

The differential cross-sections used in the present cascade model in the case of muonic hydrogen were calculated in the fully quantum mechanical close-coupling framework for $n = 2{-}5$ and in the semiclassical approximation for $n = 6{-}7$. The statistically weighted differential cross-sections were used for $n \geq 6$. In antiprotonic hydrogen, the fully quantum mechanical results are not yet available below the ns thresholds. Therefore, we used the results of the semiclassical model in the range $n = 2{-}9$ and the fixed field model for $n = 10{-}12$.

Another approximation used in this paper is related to the Auger deexcitation because the eikonal approximation [13] does not give the differential cross-section and the distribution over final l. Here we use the differential cross-section for the l-average Stark and elastic transitions and a statistical distribution over final l.

Concerning the acceleration mechanisms, the present calculations include Coulomb deexcitation through the whole cascade. For high n states, the classical-trajectory Monte Carlo method [13] was used to obtain the cross-sections of the inelastic collisions

$$(x^-p)_{n_i} + \mathrm{H}_2 \rightarrow (x^-p)_{n_\mathrm{f}} + X, X = \mathrm{H}_2,\ \mathrm{H}_2^*,\ \mathrm{H} + \mathrm{H}. \tag{4}$$

For low n, where the classical-trajectory method cannot be expected to give reliable results, we parameterize the Coulomb deexcitation cross-section as follows[1]

$$\sigma_{n\rightarrow n-1}(E_\mathrm{cm}) = c\frac{n^\gamma}{E_\mathrm{cm}}\frac{\mu_{\mu p}}{\mu_{xp}} \tag{5}$$

where E_cm is the CMS kinetic energy and $\mu_{\mu p}$ and μ_{xp} are the reduced masses of the μ^-p and the x^-p, respectively. We use the values

$$c = 1.2 \times 10^{-3} a_0^2 \text{ eV}, \tag{6}$$

$$\gamma = 3.5 \tag{7}$$

which gives a fair description of the Coulomb cross-sections of Bracci and Fiorentini [23] for $n \leq 7$.

Other calculations [24–26] predict significantly smaller Coulomb deexcitation rates than [23]. However, the rapid increase in the Coulomb cross-sections for energies approaching zero is predicted by all models. The dependence on the reduced mass is based on an estimate in [23] and

[1] The $n = 2$ state in muonic hydrogen is, however, treated differently. Coulomb deexcitation is assumed only to take place in the $2s$ state and only when the kinetic energy is below the $2p$ threshold. In this case we use the measured Coulomb deexcitation rate $\lambda_{2s\rightarrow 1s}^\mathrm{Coulomb} = 4.4 \times 10^{11} N \text{ s}^{-1}$ [12] where N is the density of the target in units of liquid hydrogen density (LHD).

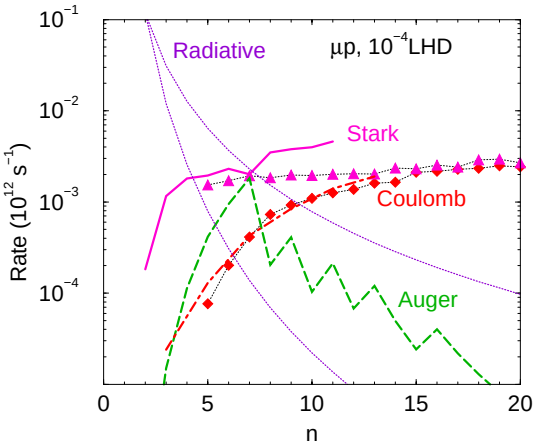

Fig. 1. The l-average rates at $T = 1$ eV for muonic hydrogen in gaseous target at 10^{-4} LHD. The Coulomb deexcitation (filled diamonds) and Stark mixing (filled triangles) rates calculated in the classical-trajectory model [13] are shown in comparison with the results of the semiclassical fixed field model for Stark mixing (solid line), Auger deexcitation (light dashed line), and nuclear absorption during collisions (dashed line) [13,16]. The Coulomb deexcitation rate from [23] is shown with a dash-dotted line. The radiative $np \to 1s$ and $n(n-1) \to (n-1)(n-2)$ rates are shown with dotted lines.

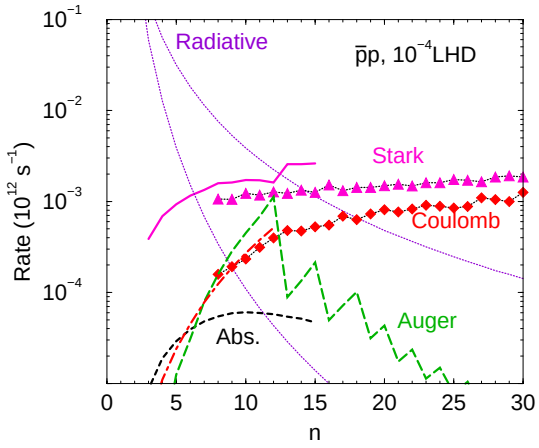

Fig. 2. The l-average rates at $T = 1$ eV for antiprotonic hydrogen in gaseous target at 10^{-4} LHD. The Coulomb deexcitation (filled diamonds) and Stark mixing (filled triangles) rates calculated in the classical-trajectory model [13] are shown in comparison with the results of the semiclassical fixed field model for Stark mixing (solid line), Auger deexcitation (light dashed line), and nuclear absorption during collisions (dashed line) [13,16]. The Coulomb deexcitation rate from equation (5) is shown with a dash-dotted line. The radiative $np \to 1s$ and $n(n-1) \to (n-1)(n-2)$ rates are shown with dotted lines.

our classical Monte Carlo calculations confirm that it is a fair approximation. We assume, furthermore, that only $\Delta n = 1$ transitions are important at low n, the distribution over final l is statistical, and the angular distribution is isotropic. As long as the mechanism responsible for Coulomb deexcitation at low n is not fully understood[2], this process enters as a major uncertainty in calculations of the kinetic energy evolution at low n. In this paper we restrict the cascade calculations to observables that are not very sensitive to the Coulomb deexcitation at low n. In the case of kinetic energy distributions this usually means low densities. Other observables, like the X-ray yields in $\mu^- p$ and cascade times, are less sensitive to the Coulomb deexcitation at low n.

Figures 1 and 2 show an overview of the cascade rates at 10^{-4} LHD in muonic and antiprotonic hydrogen calculated in the classical-trajectory model with molecular target and in semiclassical approximations with atomic target. The absorption rate in antiprotonic hydrogen shows only the absorption from the ns states during collisions. Cascade calculations show, in agreement with the experimental results [29], that absorption at densities below 10^{-3} LHD takes place mainly from the p states.

2.2 Classical-trajectory Monte Carlo model in the cascade calculations

The classical-trajectory Monte Carlo calculations have been included in the cascade calculations by using two different methods. The earlier versions of the cascade model [14] was based on the explicit use of the cross-sections [13] with the following initial conditions. A discrete set of 9 initial kinetic energies in the interval 0.05 eV $\le T \le$ 20 eV was used, and the initial principal quantum numbers were taken in the range $8 \le n_i \le 20$ for $\mu^- p$ and $13 \le n_i \le 35$ for $\bar{p}p$. For each combination of laboratory kinetic energies T and principal quantum numbers n_i, the classical trajectories were calculated using the statistical distribution in quantum number l_i as the initial condition. The differential cross-sections $\mathrm{d}\sigma/\mathrm{d}\cos\theta$ were calculated separately for the three groups of reactions:

$$n_i l_i \to \begin{cases} n_i l_i & \text{elastic} \\ n_i l_\mathrm{f}\ (l_\mathrm{f} \neq l_i) & \text{Stark} \\ n_\mathrm{f} l_\mathrm{f}\ (n_\mathrm{f} < n_i) & \text{Coulomb} \end{cases} . \qquad (8)$$

The effect of excitation and dissociation of the hydrogen molecule in Coulomb deexcitations were taken into account by distributing the final kinetic energies of the three atoms ($x^- p$ and two H) in the CMS according to the classical phase space. This approximation agrees fairly well with the calculations [13].

More detailed initial and final states are used in the present cascade model where several trajectories (21 for $\mu^- p$ and 6 for $\bar{p}p$) were calculated for each combination of the quantum numbers n_i (in the range given above) and $l_i = 0, ..., n_i - 1$, and 31 kinetic energy points in the range 0.3–32 eV. In muonic hydrogen this gives a total of 118482 trajectories. The range of impact parameters was divided into three intervals, $(0; 2a_0)$, $(2a_0; 4a_0)$, and $(4a_0; 7a_0)$, with a third of the collisions in each and the trajectories uniformly distributed in ρ^2. For each trajectory, the final quantum numbers n_f and l_f, and the final

[2] The investigation of the role of molecular resonances [27,28] is beyond the scope of this study.

laboratory kinetic energy T_f were stored. The resulting lists of transitions in the form

$$n_i\, l_i\, T_i \;\rightarrow\; n_\mathrm{f}\, l_\mathrm{f}\, T_\mathrm{f}, \tag{9}$$

with the weights of the impact parameter intervals properly taken into account, were used directly by the cascade program by redirecting the final state to the initial state of the next collision. We consider this method as more accurate than the earlier used method for cascade calculations in the upper part of the cascade.

2.3 Initial conditions

The initial conditions for the cascade calculations are defined by the initial distributions in the quantum numbers n and l and the laboratory kinetic energy T of the x^-p. In the simplest picture, the x^- is captured by the proton after ionization of the hydrogen atom in a state with large overlap with the $1s$ electron wave function; this gives $n_i \sim \sqrt{\mu_{xp}/m_e}$ (~ 14 for muonic and ~ 30 for antiprotonic hydrogen). More elaborate calculations, which take the molecular structure of the target into account, predict distributions in the initial n which peak at lower values: for example, the maximum at $n = 11$ for muonic hydrogen [30]. A shift towards lower initial n values is also found in [31]. The new experimental data on muonic hydrogen kinetic energy distributions from PSI are sensitive to the initial distributions as discussed below in Section 3.1.4.

Unless otherwise indicated, we use the initial principal quantum number $n_i = 14$ for μ^-p and $n_i = 30$ for $\bar{p}p$ and the initial kinetic energy given by a Maxwell distribution

$$w(T_i) = 3\sqrt{\frac{3T_i}{2\pi T_0}}\exp\left(-\frac{3T_i}{2\pi T_0}\right) \tag{10}$$

with $T_0 = 0.5$ eV. In all cases the l_i distribution is statistical.

3 Results

3.1 Muonic hydrogen

The cascade calculations in muonic hydrogen have been done in the density range $(10^{-8}{-}1)$ LHD using various initial conditions. The results are compared with the experimental data for the metastable $2s$ population, X-ray yields, cascade times, and kinetic energy distributions [12,32–37,39,43].

3.1.1 The metastable 2s fraction

The metastable $2s$ state of muonic hydrogen is of great interest because it allows, under certain conditions, to measure the μ^-p Lamb shift, $2s - 2p$, from which the proton charge radius can be determined with high precision [38]. The feasibility of this experiment, presently in progress at PSI [39], relies on a sizeable fraction of muonic hydrogen atoms in the $2s$ state with a sufficiently long lifetime. In the absence of collisions, the lifetime of the $2s$ state is determined by the muon lifetime ($\tau_\mu = 2 \times 10^{-6}$ s) as the rate for the $2s \rightarrow 1s$ two-photon transition is negligibly small. At target densities above 10^{-7} LHD, the lifetime of the $2s$ state depends on the kinetic energy of the μ^-p. Below the $2p$ threshold, $T_{2p} = 0.3$ eV, the $2s$ state is long-lived because $2s \rightarrow 2p$ Stark transitions followed by the fast radiative deexcitation $2p \rightarrow 1s$ are energetically forbidden. The induced radiative transition can, however, occur during collisions, see [41,42] and below. For kinetic energies above the $2p$ threshold the collisions with the target molecules lead to a competition between deceleration and depletion *via* $2s \rightarrow 2p$ Stark transitions followed by the $2p \rightarrow 1s$ radiative transition. The *metastable* $2s$ *fraction*, R_{2s}, is defined as the fraction of all created μ^-p atoms which end up in the $2s$ state with kinetic energies below T_{2p}.

Before we present the results of our full cascade model, it is illuminating to consider the problem of the metastable $2s$ fraction in a simplified framework. The metastable $2s$ fraction consists of the μ^-p that are formed with kinetic energies below T_{2p} and those that are formed with kinetic energies above T_{2p} but slow down below threshold due to elastic collisions. The median kinetic energy at 1 mbar is 1.5 eV [12], so the deceleration process is important. This leads to the definition of the *surviving metastable fraction*, $f(T)$, which is the probability that the μ^-p atom in the $2s$ state with initial kinetic energy T reaches energies below the $2s$ threshold by slowing down in elastic collisions [21].

In the approximation of continuous energy loss the evolution in the kinetic energy is given by

$$-T^{-1}\frac{\mathrm{d}T}{\mathrm{d}t} = 2\frac{M_{\mu p}M_\mathrm{H}}{(M_{\mu p}+M_\mathrm{H})^2}Nv\sigma^\mathrm{tr}_{2s\rightarrow 2s}(T) \tag{11}$$

where $M_{\mu p}$ and M_H are the masses of the μ^-p and the H, respectively, v the velocity of the μ^-p, and $\sigma^\mathrm{tr}_{2s\rightarrow 2s}(T)$ the transport cross-section [16]. Equation (11) was used by Carboni and Fiorentini [40] to get the following estimate of the surviving metastable fraction

$$f(T) = \exp\left(-\frac{(M_{\mu p}+M_\mathrm{H})^2}{2M_{\mu p}M_\mathrm{H}}\int_{T_{2p}}^{T}\frac{\sigma_{2s\rightarrow 2p}(T')}{T'\sigma^\mathrm{tr}_{2s\rightarrow 2s}(T')}\mathrm{d}T'\right). \tag{12}$$

It was found that a sizeable fraction of $(\mu^-p)_{2s}$ atoms formed at kinetic energies below 1.3 eV slows down below threshold.

To provide a more realistic treatment of the evolution in kinetic energy we use a Monte Carlo program based on the differential cross-sections for the four processes $2s \rightarrow 2s$, $2s \rightarrow 2p$, $2p \rightarrow 2s$ and $2p \rightarrow 2p$. In addition to the collisional processes, the $2p \rightarrow 1s$ radiative transition is also included in the calculation. The fate of a μ^-p formed in the $2s$ state with kinetic energy T is thus either to undergo $2p \rightarrow 1s$ radiative transition after the Stark mixing $2s \rightarrow 2p$ or to end up in the $2s$ state with kinetic energy below the threshold with probability $f(T)$.

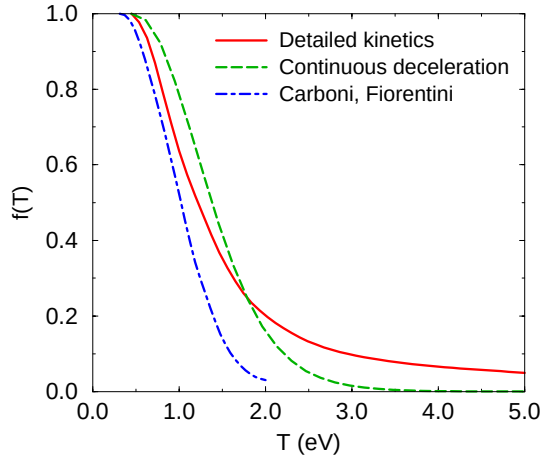

Fig. 3. Energy dependence of the surviving metastable fraction $f(T)$ of the $2s$ state of muonic hydrogen. The result of the detailed kinetics calculations (solid line) is shown in comparison with the approximation of continuous deceleration (12) (dashed line) and the result of Carboni and Fiorentini [40].

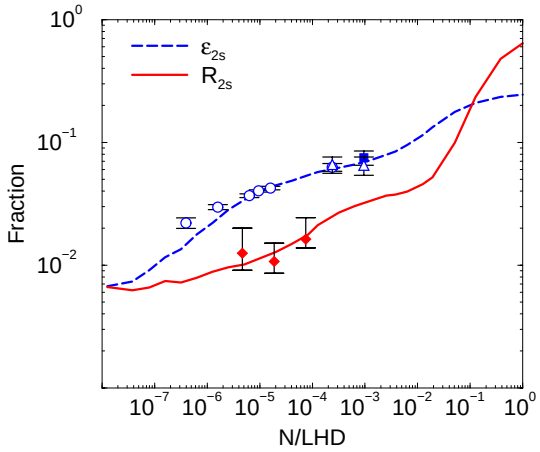

Fig. 4. *Ab initio* cascade calculation of the $2s$ arrival probability, ϵ_{2s} (dashed line), in comparison with the values derived from X-ray measurements: [34] (circles), [32] (triangles), and [33] (filled square). The solid line shows the the metastable $2s$ fraction, R_{2s}; the corresponding experimental data (filled diamonds) are from [12].

Figure 3 shows the surviving metastable fraction, $f(T)$, calculated with the Monte Carlo program for target density 10^{-6} LHD $< N < 10^{-2}$ LHD. The approximation (12) gives somewhat higher values for the survival probability than the exact kinetics calculation at $T < 1.4$ eV. The Monte Carlo results at high energies ($T > 1.5$ eV) are significantly larger than those obtained from equation (12) where continuous energy loss is assumed. The reason is that there is a significant contribution to $f(T)$ from large-angle scattering. The result of [40] is considerably smaller than the present result due to differences in the cross-sections and the fact that in [40] the molecular hydrogen mass was used instead of the atomic one in order to get the correct value for the threshold. By using the surviving metastable fraction $f(T)$, the measured kinetic energy distributions on arrival in the $1s$ state [12], and the $2s$ arrival probability[3] [34], one finds the metastable $2s$ fraction to be $\sim 1\%$ in the pressure region 0.06−16 mbar as discussed in [12].

After reaching thermal energies the $(\mu^- p)_{2s}$ atoms may undergo radiative deexcitation during collisions because of the Stark effect [41,42]:

$$(\mu^- p)_{2s} + \mathrm{H} \to (\mu^- p)_{2s-2p} + \mathrm{H} \to (\mu^- p)_{1s} + \gamma(1.9\ \mathrm{keV}) + \mathrm{H}. \quad (13)$$

The radiative quenching of thermal $(\mu^- p)_{2s}$ atoms would result in delayed K_α X-rays. However, the experiments [32–34] have not observed this effect. This apparent contradiction was recently resolved by the $\mu^- p$ diffusion experiment [12,43] where 0.9 keV $(\mu^- p)_{1s}$ atoms, resulting from the Coulomb deexcitation process

$$(\mu^- p)_{2s} + \mathrm{H} \to (\mu^- p)_{1s}(0.9\ \mathrm{keV}) + \mathrm{H}(1.0\ \mathrm{keV}), \quad (14)$$

were found. The measured non-radiative quenching rate is about 2 $\mu\mathrm{s}^{-1}$ at 1 mbar [12,43] which is more than an order of magnitude larger than the theoretical predictions for the radiative quenching rate [41,42].

The $2s$ arrival probability, ϵ_{2s}, and metastable $2s$ fraction calculated in the ESCM with the initial conditions specified in Section 2.3 is shown in Figure 4. The calculated $2s$ arrival probability is in good agreement with the experimental data obtained from measurements of X-ray yields [32–34]. The arrival probability ϵ_{2s} increases steadily with increasing density from 1% at 10^{-7} LHD to 25% in liquid hydrogen. This behavior has a simple qualitative explanation: at the lowest densities the cascade proceeds purely radiatively from high n values. As only $\Delta l = 1$ transitions are allowed, the circular states are predominantly populated for low n. The majority of exotic atoms, therefore, go through the radiative $2p \to 1s$ transition without reaching the $2s$ state. With the density increasing the Stark mixing becomes efficient at lower n levels and more $np \to 2s$ radiative transitions take place. In liquid hydrogen, ϵ_{2s} is given by the statistical weight of the $2s$ state.

In the density range 10^{-7}−10^{-4} LHD, the calculated metastable fraction increases from 0.7% to 2%, and this is in perfect agreement with the experimental result [12] obtained in measurements of 0.9 keV $(\mu^- p)_{1s}$ atoms. The metastable fraction grows slowly with density until about 0.01 LHD. Above 0.01 LHD the growth becomes faster and R_{2s} reaches 65% in liquid hydrogen. The large metastable fraction at high densities is a consequence of the dominance of the slowing down in $2l_i \to 2l_\mathrm{f}$ collisions over the radiative $2p \to 1s$ deexcitation.

Figure 5 shows the time dependence of the $2s$ population, P_{2s}, at 1 mbar. The $2s$ population grows rapidly

[3] The $2s$ arrival probability is the fraction of formed exotic atoms that arrives at the $n = 2$ level in the $2s$ state. It can be estimated from measurements of K X-ray yields using the known $Y_{np\to 2s}/Y_{np\to 1s}$ branching ratios.

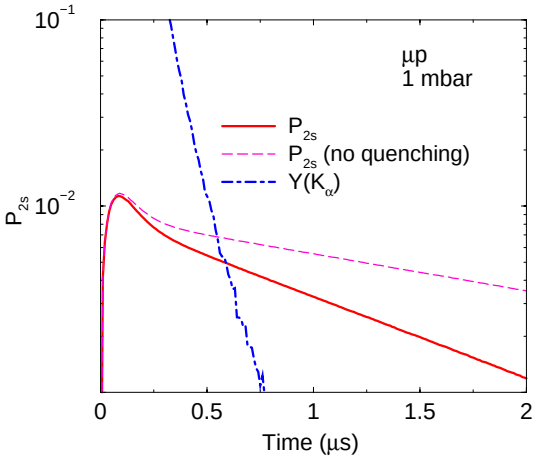

Fig. 5. The time dependence of the $2s$ population, P_{2s} (solid line), of muonic hydrogen at 1 mbar. The thin dashed line shows P_{2s} calculated without collisional quenching of the metastable $2s$ state. The dashed-dotted line shows the distribution of the K_α X-rays in units of μs^{-1}.

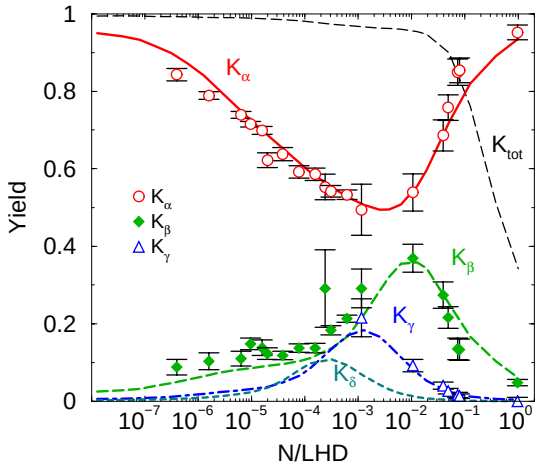

Fig. 6. The density dependence of the relative X-ray yields, K_α, K_β, and K_γ, and the absolute total yield $K_{\rm tot}$ in muonic hydrogen. The experimental data are from [34–36].

with time in the beginning of the cascade and reaches a maximum of 1.2% after 0.1 μs. The development at later times clearly shows the two components of P_{2s}. The short-lived component consists of the $\mu^- p$ atoms with kinetic energies above the threshold, T_{2p}, which go through the $2s \rightarrow 2p$ Stark transition followed by the radiative deexcitation. The long-lived component consists of the metastable $(\mu^- p)_{2s}$. The atomic cascade is essentially terminated after 0.7 μs: the $\mu^- p$ atoms are either in the $1s$ state or the metastable $2s$ state. The metastable $2s$ state is quenched non-radiatively (14) with a rate at 1 mbar of about 4 times the rate for muon decay.

The results in Figure 5 were calculated under the assumption that all $\mu^- p$ atoms were formed at the same time. In reality, the muons are injected into the target, slow down in collisions with the H_2 molecules, and are then captured by a proton. Having to go through the slowing down process means that the time of formation is given by a density dependent distribution — the so-called stop time distribution. The measured stop time at 1 mbar is $\tau_{\rm stop} = 0.48 \pm 0.13$ μs [12] which, when taken into account, does not change the overall features of Figure 5 except for the time offset.

The results for the $2s$ population are extremely important for the $2s - 2p$ Lamb shift experiment [38,39]. In this experiment, a laser will be used to induce $2s \rightarrow 2p$ transitions which are followed by the fast radiative $2p \rightarrow 1s$ deexcitation. The K_α X-rays are detected in coincidence with the laser pulse and the $2s - 2p$ energy splitting is then deduced from the laser wavelength corresponding to the strongest K_α signal. This laser experiment is feasible provided the $2s$ population is not too small and the K_α background produced by the cascade is negligible. These conditions are fulfilled at very low densities (around a few mbar) after a short delay time as discussed above.

3.1.2 X-ray yields

The calculated relative X-ray yields for the $\mu^- p$ atom are shown in comparison with the experimental data in Figure 6. The agreement between theory and experiment is good for the K_α, K_β, and K_γ yields. The relative K_α yield is higher than 90% at 10^{-7} LHD, it decreases with the density increasing and reaches a minimum of 50% at 2×10^{-3} LHD. Above 2×10^{-3} LHD the relative K_α yield increases and ends at 94% in liquid hydrogen. The opposite behavior is seen in the other K yields. They start out close to zero at 10^{-7} LHD, increase with the density and reach their maxima (at 0.01 LHD for K_β, 10^{-3} LHD for K_γ, and 3×10^{-4} LHD for K_δ), and, with the exception of K_β, practically vanish at LHD. The density dependence of the yields can be explained qualitatively in a way similar to the discussion of the $2s$ population above. At 10^{-7} LHD the cascade is almost purely radiative and proceeds at low n through the circular states, so that almost all $\mu^- p$ atoms go through the radiative $2p \rightarrow 1s$ transition whereas the transitions $np \rightarrow 1s$ with $n > 2$ are much weaker. With increasing density the Stark mixing becomes more efficient and leads to higher populations of the np states with $n > 2$. This explains the increase in the relative $K_{\geq\beta}$ yields and consequently also the decrease in K_α. The decrease in the $K_{\geq\beta}$ yields for higher densities is due to the collisional deexcitation $n \rightarrow n - 1$ which begin to dominate the radiative transitions.

At high density, a significant fraction of the $\mu^- p$ atoms slows down at the very end of the cascade before reaching the ground state and populate the metastable $2s$ state with high probability ($R_{2s} \approx 0.65$ in liquid hydrogen) as discussed above. This makes the ratio of K_α and K_β yields in liquid hydrogen very sensitive to the quenching mechanism of the $2s$ state. As demonstrated in Figure 7, the X-ray data favor non-radiative quenching (14) in agreement with the recent experiment on direct search for the metastable $2s$ state [12]. It would be very important to check this result directly by measuring the *absolute*

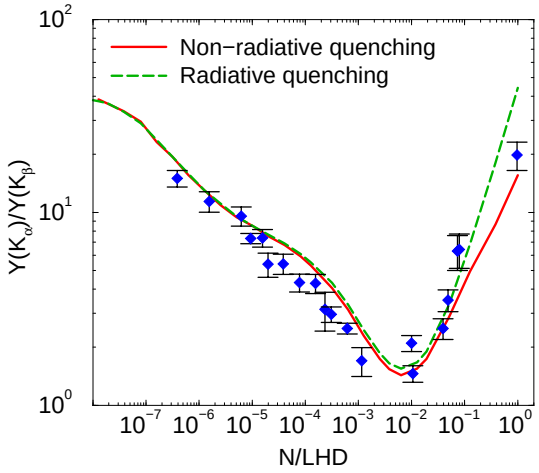

Fig. 7. The ratio of the K_α and K_β yields for the non-radiative (solid line) and radiative (dashed line) quenching of the $2s$ state. The data are from [34–37].

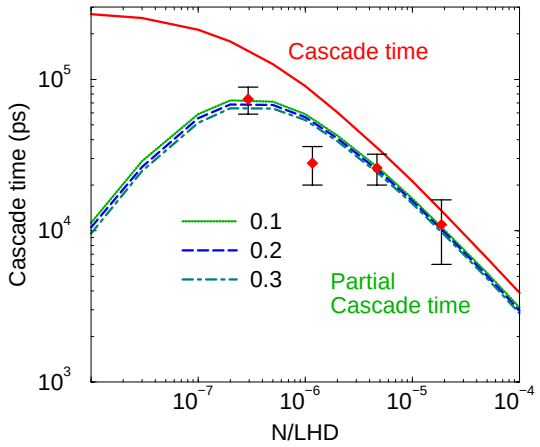

Fig. 8. The calculated cascade time and the partial cascade time in $\mu^- p$ *vs.* density. The partial cascade times are shown for different values of the parameter δ. The experimental data are from [12].

X-ray yield in liquid hydrogen: the non-radiative quenching leads to a significant suppression of the X-ray yield: $Y(K_{\rm tot}) \approx 0.35$.

3.1.3 Cascade time

The cascade time in muonic hydrogen at low pressures (0.25–16 mbar) was measured recently in the $(\mu^- p)_{1s}$ diffusion experiment at PSI [12]. The experimentally measured value is the so-called *partial cascade time* that is defined as the time between formation of the $\mu^- p$ and the last "significant" collision during the cascade, and is, therefore, smaller than the cascade time usually defined as the time between formation and arrival in the ground state. The exact definition of the measured partial cascade time is contained in a non-trivial way in the data analysis program of [12]; we can approximate it by defining a collision to be "significant" if the relative change in $\mu^- p$ kinetic energy is larger than δ which we vary in the range 0.1−0.3. The calculated cascade time and partial cascade time are shown in Figure 8 in comparison with the experimental data [12]. Whereas the cascade time grows as the pressure decreases and eventually reaches the purely radiative cascade time, the partial cascade time reaches its maximum at 2×10^{-7} LHD and vanishes at zero pressure where there are no collisions. The calculated partial cascade time depends only weakly on δ, and our results are in good agreement with the experiment.

The n dependence of the partial cascade time at 0.25 and 4 mbar is shown in Figure 9. At 4 mbar, the partial cascade time depends only weakly on the initial n and is in perfect agreement with the experimental result for $n > 10$. The calculated partial cascade time at 0.25 mbar has a moderate dependence on n and agrees with the experiment for $n = 13$−15. Though this seems to support the simple picture of the $\mu^- p$ atoms being formed with $n \sim 14$, the models that predict lower values for the initial n can also be consistent with the experiment because

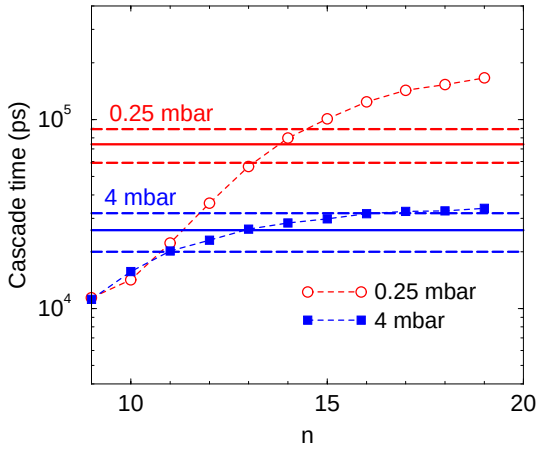

Fig. 9. The partial cascade time as a function of the initial n at 0.25 mbar and 4 mbar. The average initial energy is 0.5 eV and the parameter $\delta = 0.1$. The experimental data are from [12].

the n distributions usually have tails that extends up to high values. For example, using the the n distribution for molecular target from [30] we obtain the partial cascade time $\tau_{\rm casc} = 60$ ns at 0.25 mbar in good agreement with the measured $\tau_{\rm casc} = 74 \pm 15$ ns [12].

3.1.4 Kinetic energy distribution

The kinetic energy distribution of muonic hydrogen atoms on arrival in the $1s$ state has been obtained by analyzing $\mu^- p$ diffusion times in hydrogen gas [9,11,12,39]. The integrated kinetic energy distribution[4] of muonic hydrogen

[4] The reason for using the integrated instead of the differential kinetic energy distribution, $w(T)$, is that neighboring energy bins are highly correlated in the experimental analysis.

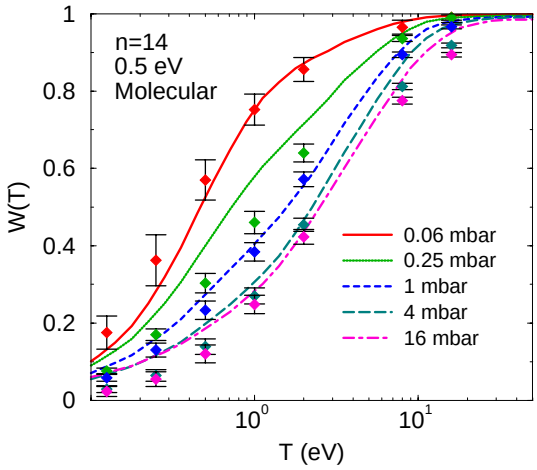

Fig. 10. The integrated energy distribution $W(T)$ of the $\mu^- p$ atom at the end of the cascade for initial conditions: $n_i = 14$ and $T_0 = 0.5$ eV. The data are from [12].

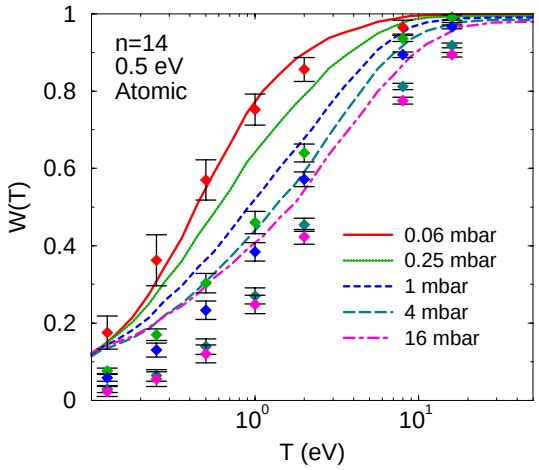

Fig. 11. The integrated energy distribution $W(T)$ of the $\mu^- p$ atom at the end of the cascade for initial conditions: $n_i = 14$ and $T_0 = 0.5$ eV. The classical-trajectory calculations at $n > 7$ were done for *atomic* target. The data are from [12].

on arrival in the $1s$ state

$$W(T) = \int_0^T w(T')\mathrm{d}T' \qquad (15)$$

was determined recently at PSI [12,39]. The results obtained in the pressure range 0.06−16 mbar offer a unique possibility to study the formation of the $\mu^- p$ and the initial stages of the cascade. Figure 10 shows the integrated kinetic energy distribution calculated in the cascade model and the experimental data from [12]. The data at 0.06 mbar are sensitive mainly to the initial energy distribution. With the density increasing, the role of the collisional processes grows, and the final distribution becomes more energetic due to acceleration at the beginning of the cascade. The results of the cascade calculations are in a fair agreement with the data for the initial conditions specified in Section 2.3. The Coulomb transitions with $\Delta n > 1$ were found to be essential for explaining the observed increase in kinetic energy with increasing pressure in agreement with the earlier analysis [11]. Similar cascade calculations using the trajectories of $\mu^- p$ collisions with *atomic* hydrogen, where the collisions with $\Delta n = 1$ dominate the collisional deexcitation, predict a much weaker increase in kinetic energy as shown in Figure 11.

The cascade calculations predict, independent of the initial n, significantly smaller fractions of $(\mu^- p)_{1s}$ atoms with high kinetic energies ($T \geq 8$ eV) at pressures above 4 mbar than the experimental data.

Figure 12 shows the density dependence of $W(1\text{ eV})$ and $W(8\text{ eV})$. The calculated sub-1 eV fraction, $W(1\text{ eV})$, decreases from 80% at 0.06 mbar to 30% at 16 mbar in good agreement with the experimental data [12]. The $\mu^- p$ atoms with energies above 8 eV are produced during the cascade in Coulomb transitions. The present calculations predict an increase in $W(T \geq 8\text{ eV})$ with the pressure from 1% at 0.06 mbar to 17% at 16 mbar. The predicted curves agree with the experimental results in the range 0.06−1 mbar whereas the measured high energy fraction is substantially larger than the calculated one for pressures

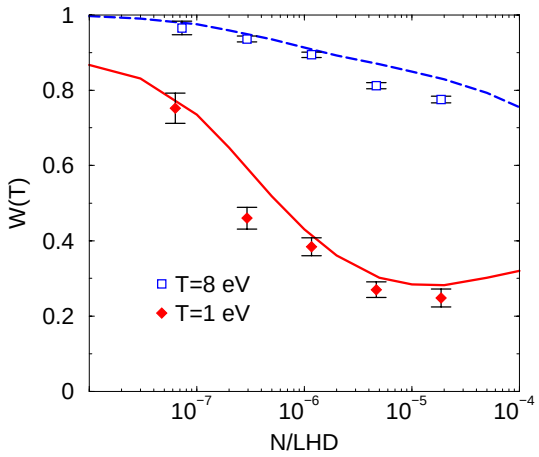

Fig. 12. The density dependence of the integrated energy distributions $W(1\text{ eV})$ and $W(8\text{ eV})$ of the $\mu^- p$ atom for initial conditions: $n_i = 14$ and $T_0 = 0.5$ eV. The data are from [12].

above 4 mbar: for example $W(T \geq 8\text{ eV}) = (22.5 \pm 0.9)\%$ at 16 mbar [12]. The measured increase in the high energy fraction of $(\mu^- p)_{1s}$ atoms cannot be reproduced in the current cascade model for any initial distribution.

Figures 13, 14, and 15 show the density dependence of the median kinetic energy on arrival in the ground state for different initial conditions. With the density increasing the calculated median energies grow and reach 2.5 eV around 10^{-5} LHD. Above 10^{-5} LHD, the median energies remain nearly constant up to 2×10^{-4} LHD where they start to grow again. The shape of the curves can be explained as follows. The increase in the median energies at low densities is produced in the classical domain ($n > 7$) where the acceleration due to Coulomb transitions with $\Delta n = 1{-}5$ is more efficient than the slowing down. The plateau is due to the dominance of Auger deexcitation at medium n which become important around the density 10^{-5} LHD. The increase in the median energy in the uppermost part of the shown density range is produced

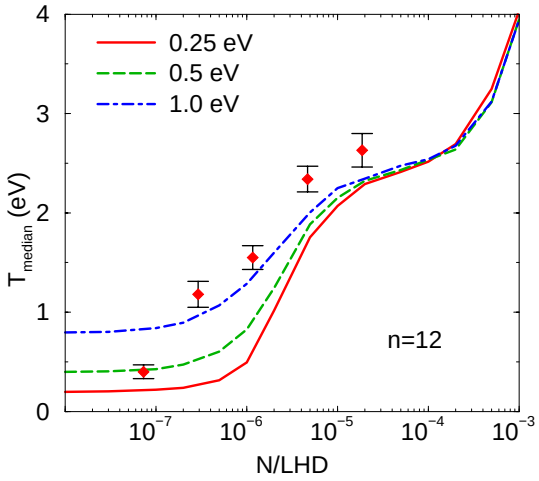

Fig. 13. The density dependence of the median kinetic energy of the $\mu^- p$ at the end of the cascade for different initial average kinetic energies and $n_i = 12$. The data are from [12,44].

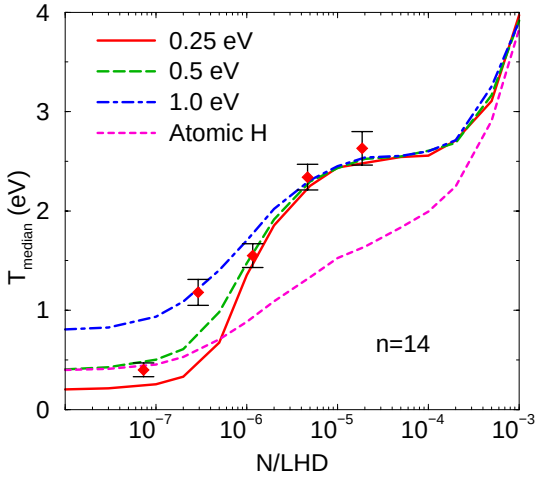

Fig. 14. The density dependence of the median kinetic energy of the $\mu^- p$ at the end of the cascade for different initial average kinetic energies and $n_i = 14$. The result for atomic target is shown for $T_0 = 0.5$ eV. The data are from [12,44].

by the Coulomb transitions at $n < 8$. For densities larger than 10^{-4} LHD, the initial kinetic energy is almost forgotten because of the many collisions during the cascade, and the kinetic energy distribution at the end of the cascade is determined by the competition between acceleration and deceleration during the cascade.

The measured density dependence of the median kinetic energy is well reproduced with the initial conditions: $T_0 = 0.5$ eV and $n_i = 14$ or $T_0 = 0.25$ eV and $n_i = 16$. For $n_i = 12$ (Fig. 13) the initial acceleration appears to be weaker and the agreement with the experimental result is worse. The molecular structure of the target is essential for explaining the data. Calculations with the CMC trajectories for *atomic* hydrogen lead to a too weak increase in the median energy compared to the experiment.

We estimate the statistical errors due to the finite number of CMC trajectories by dividing the 21 complete sets

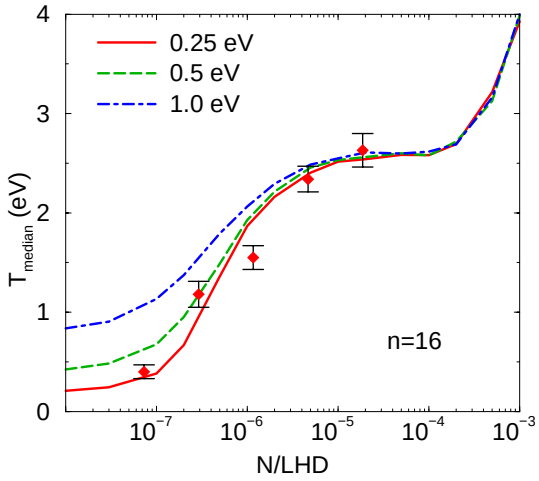

Fig. 15. The density dependence of the median kinetic energy of the $\mu^- p$ at the end of the cascade for different initial average kinetic energies and $n_i = 16$. The data are from [12,44].

Table 2. Median kinetic energy and integrated kinetic energy in muonic hydrogen calculated in the ESCM with statistical errors. The experimental results are from [12,44].

Observable	ESCM	Exp.
$T_{\rm median}(1$ mbar)	1.57 ± 0.03 eV	1.55 ± 0.12 eV
$T_{\rm median}(16$ mbar)	2.50 ± 0.14 eV	2.63 ± 0.17 eV
$W(16$ eV) at 16 mbar	0.958 ± 0.004	0.894 ± 0.006

of trajectories into 7 subsets and calculate the observables using each subset. The results for the median kinetic energy and the integrated kinetic energy shown in Table 2 does not change the conclusions reached above: the ESCM gives a good description of the experimental data for moderate energies but is unable to explain the observed high energy fraction.

3.2 Antiprotonic hydrogen

The present study of the atomic cascade in antiprotonic hydrogen was focused on the experimental data obtained at low density [45–50].

3.2.1 X-ray yields

The calculated X-ray yields are in a good agreement with the data [46–49] as shown in Figures 16 and 17. In addition to the data on absolute X-ray yields, there are more precise measurements of relative yields, see Table 3. The theoretical results are in fair agreement with the data as all the calculated ratios deviate less than 50% from the experimental results. This is a significant improvement in comparison with the calculations in the Borie-Leon model reported in [48]: the two standard tuning parameters $k_{\rm Stk}$ and T were fixed by fitting the absolute L_α yields but the predictions of the model for ratios involving L_δ were a factor of 3−5 larger than the experimental data. We stress

Table 3. Relative X-ray yields in $\bar{p}p$.

Observable	Pressure	ESCM	Exp.	References
$Y(K_\alpha)/Y(L_\alpha)$	20 mbar	0.0179	0.0176 ± 0.0016	[51]
$Y(L_{\rm tot})/Y(L_\alpha)$	20 mbar	1.56	1.45 ± 0.05	[51]
$Y(L_\alpha)/Y(L_\beta)$	30 mbar	5.0	7.1 ± 0.7	[48]
$Y(L_\alpha)/Y(L_\gamma)$	30 mbar	13.2	20.6 ± 2.0	[48]
$Y(L_\alpha)/Y(L_\delta)$	30 mbar	22.6	23.9 ± 2.6	[48]
$Y(L_\alpha)/Y(L_{\rm tot})$	30 mbar	0.62	0.75 ± 0.08	[48]
$Y(L_\beta)/Y(L_\gamma)$	30 mbar	2.7	2.9 ± 0.2	[48]
$Y(L_\beta)/Y(L_\delta)$	30 mbar	4.6	3.4 ± 0.2	[48]
$Y(L_\gamma)/Y(L_\delta)$	30 mbar	1.7	1.2 ± 0.1	[48]

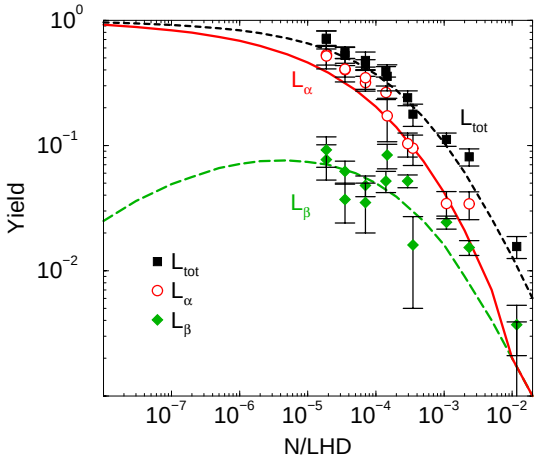

Fig. 16. The density dependence of the absolute L X-ray yields in antiprotonic hydrogen. The experimental data are from [46–49].

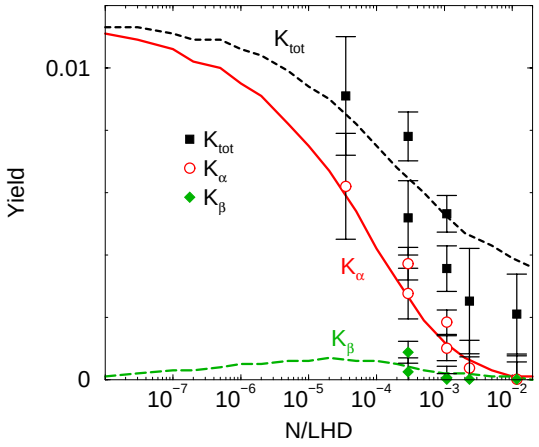

Fig. 17. The density dependence of the absolute K X-ray yields in antiprotonic hydrogen. The experimental data are from [46–49].

that our results were obtained without employing any cascade tuning parameters. Figure 18 shows an example of the X-ray profile of the K lines at 10^{-3} LHD. Because of the hadronic broadening of the $1s$ state, only the K_α line is clearly separable from the rest of the K lines of which the $9p \rightarrow 1s$ transition has the highest intensity. The relatively large contribution to the K yield from high n states

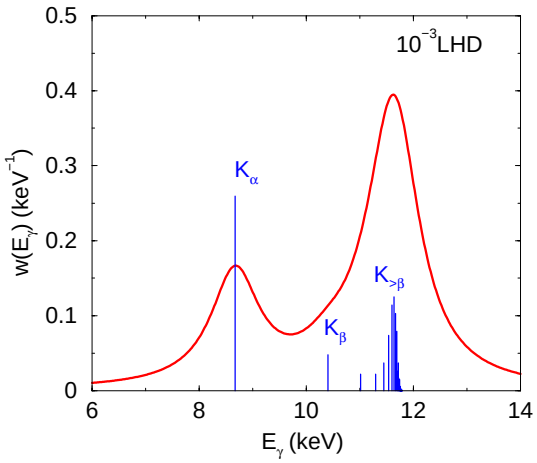

Fig. 18. The K line profile in antiprotonic hydrogen at 10^{-3} LHD.

is due to the strong absorption in the excited states which prevents most of the $\bar{p}p$ atoms from reaching the low n states.

3.2.2 Cascade time

The density dependence of the cascade time is shown in Figure 19. Our result is in good agreement with the data [45] except for the data point at 150 mbar where our model predicts significantly shorter cascade time. The agreement for pressures up to 10 mbar can be considered as an important confirmation of the dominance of the Coulomb transitions with large changes in the principal quantum number n in the upper part of the atomic cascade. The earlier calculations [5] predicted much higher cascade times in variance with the experimental data.

The dependence of the cascade time at 3.4 and 9.8 mbar on the initial n is shown in Figure 20. There is good agreement with the experimental result [45] in the range $n = 25{-}35$. Calculations also show that the calculated cascade times depend only weakly on the initial kinetic energy.

3.2.3 Kinetic energy distributions

In the upper part of the cascade most of the $\bar{p}p$ atoms are accelerated to energies of several eV in the Coulomb

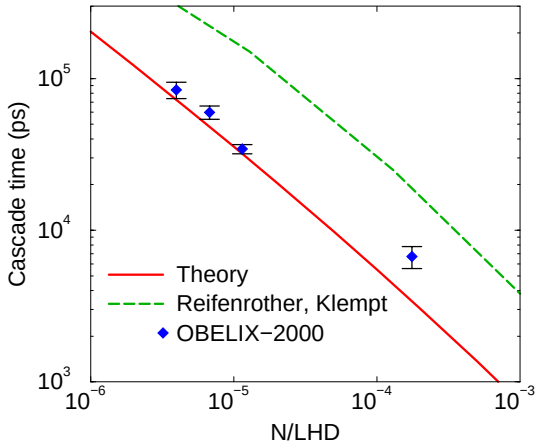

Fig. 19. The density dependence of the cascade time in antiprotonic hydrogen. The experimental data are from [45].

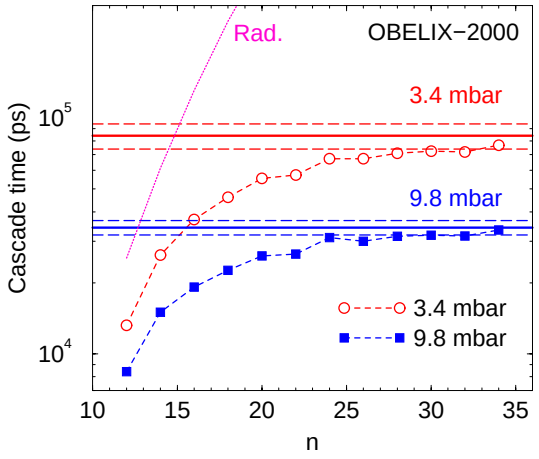

Fig. 20. The dependence of the cascade time in $\bar{p}p$ at 3.4 and 9.8 mbar on the initial state n. The initial average kinetic energy is 0.5 eV. The cascade time for a purely radiative cascade is shown for comparison. The experimental data are from [45].

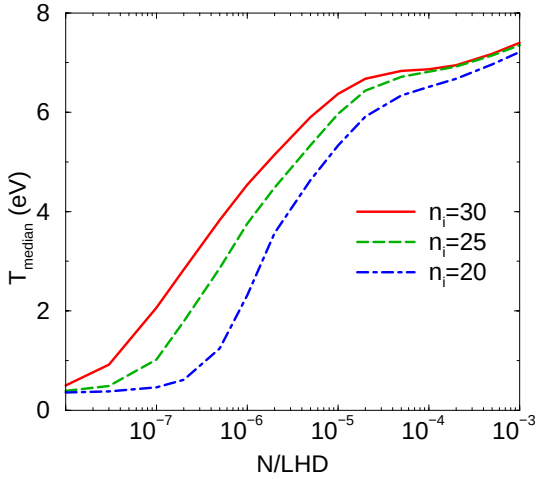

Fig. 21. The density dependence of the median energy at the instant of nuclear absorption in antiprotonic hydrogen for initial $n = 20, 25, 30$.

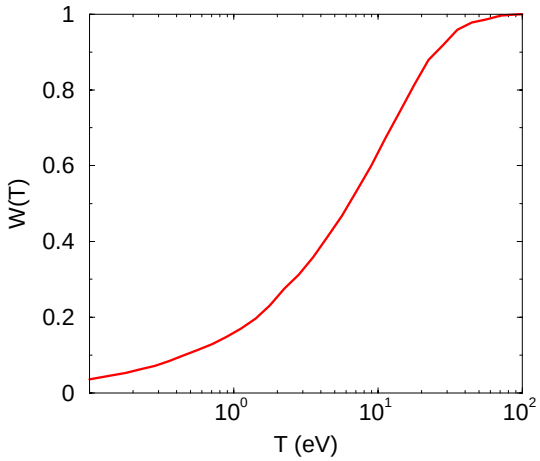

Fig. 22. The calculated integrated energy distribution of $\bar{p}p$ at the instant of the $3d \rightarrow 2p$ transition at 22 mbar.

transitions with $\Delta n > 1$. Figure 21 shows the density dependence of the median energy at the instant of nuclear absorption calculated for initial $n = 20, 25, 30$. The shape of the curves are similar to those of muonic hydrogen but the energy is higher. The median energy increases rapidly with increasing density and reaches 6−7 eV at 10^{-5} LHD. At higher densities the dominance of the Auger transitions at intermediate n prevents further increase until the Coulomb deexcitation at low n becomes important.

3.2.4 Doppler broadening of the L lines

The acceleration processes during the atomic cascade lead to a sizeable Doppler broadening of the L lines. Figure 22 shows the integrated energy distribution of the $\bar{p}p$ atoms at the instant of the $3d \rightarrow 2p$ transition in a gaseous target of 22 mbar, the median energy being about 6.5 eV. The corresponding Doppler broadening of the $3d \rightarrow 2p$ line profile is shown in Figure 23; the effect gives a significant contribution to the width and must, therefore, be taken into account in the analysis of the X-ray spectra. In the data analysis in [50] it was assumed that the $\bar{p}p$ atoms were thermalized due to elastic and Auger collisions.

4 Conclusions

Using the new results for the collisional processes [13,16], the atomic cascades in muonic and antiprotonic hydrogen have been studied in detail. The cascade calculations have been done in the extended standard cascade model which describes the evolution in the quantum numbers n and l and the kinetic energy from the very beginning of the cascade. By taking deceleration and acceleration during the cascade into account, observables can be predicted reliably without the need for any cascade tuning parameters. The extended standard cascade model successfully describes a number of experimental results: X-ray yields, cascade times, and kinetic energy distributions.

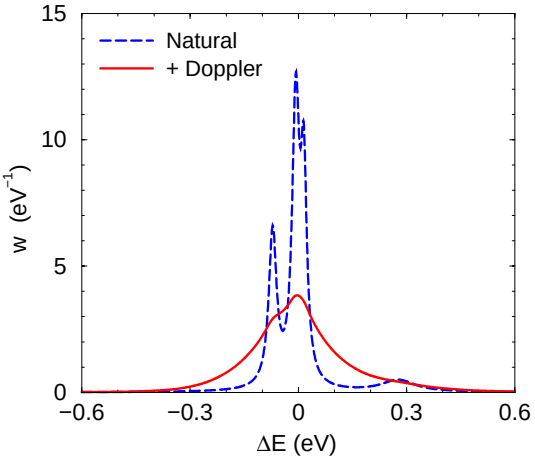

Fig. 23. The natural L_α line profile in $\bar{p}p$ (dashed line) in comparison with the Doppler broadened line profile at 22 mbar (solid line). For the electromagnetic hyperfine splitting we use the result of Boucard and Indelicato [50]. The hadronic splitting and broadening are taken from the DR1 model of [52].

The results of the cascade calculations for muonic and antiprotonic hydrogen can be summarized as follows:

– *muonic hydrogen.* The calculated X-ray yields in muonic hydrogen are in good agreement with the data. The measured ratio of the K_α and K_β yields in liquid hydrogen can be reproduced only if the non-radiative quenching of the metastable $2s$ state is dominant. The calculated increase in the $(\mu^- p)_{1s}$ median kinetic energy with the density is in agreement with the data [12] for the initial conditions corresponding to kinetic energies around 0.5 eV and principal quantum number $n \approx 14$. The molecular structure of the target is essential for explaining the data on the density dependence of the kinetic energy distribution at the end of the cascade;

– *antiprotonic hydrogen.* The calculated K and L X-ray yields in antiprotonic hydrogen are in good agreement with the data. The calculated cascade time is in good agreement with the data. For the first time, a good description of the data is obtained without using any phenomenological tuning parameters. The fast collisional deexcitation at high n calculated in the classical-trajectory model was found to be very important for explaining the short cascade times measured by the OBELIX collaboration [45]. The acceleration of the $\bar{p}p$ during the initial stages of the cascade predicted by our cascade model results in a significant Doppler broadening of the L lines. This must be taken into account when hadronic widths and shifts are obtained from the measured line profiles.

Some experimental data cannot be explained in the present version of the ESCM even with taking the uncertainties in the cross-sections into account. The problem of the high energy fraction of the kinetic energy distribution in muonic hydrogen deserves special attention in future studies: the ESCM predicts a much smaller fraction of $\mu^- p$ atoms with energies above 16 eV at 4 and 16 mbar than the experimental result [12]. This disagreement indicates that some processes beyond the ESCM are important. Candidates under discussion are the hybrid Auger-Coulomb transitions [53] and the resonant formation of molecular states [28].

Future development of the ESCM will consist of calculations of the above mentioned processes and their inclusion in the cascade model. At the same time the cascade calculations can be easily extended to cover exotic deuterium atoms and H–D mixtures. Further critical tests of the current theory of the atomic cascade will greatly benefit from the results of the experiments on the precision spectroscopy of pionic and muonic hydrogen, presently in progress at PSI.

We thank F. Kottmann, L. Simons, D. Taqqu, R. Pohl, and D. Gotta for fruitful and stimulating discussions.

References

1. M. Leon, H.A. Bethe, Phys. Rev. **127**, 636 (1962)
2. V.E. Markushin, Phys. Rev. A **50**, 1137 (1994)
3. V.E. Markushin, Hyperf. Interact. **119**, 11 (1999)
4. E. Borie, M. Leon, Phys. Rev. A **21**, 1460 (1980)
5. G. Reifenröther, E. Klempt, Nucl. Phys. A **503**, 885 (1989)
6. E.C. Aschenauer *et al.*, Phys. Rev. A **51**, 1965 (1995)
7. T.P. Terada, R.S. Hayano, Phys. Rev. C **55**, 73 (1997)
8. J.E. Crawford *et al.*, Phys. Lett. B **213** 391 (1988); Phys. Rev. D **43**, 46 (1991)
9. D.J. Abbott *et al.*, Phys. Rev. A **55**, 165 (1997)
10. A. Badertscher *et al.*, Europhys. Lett. **54**, 313 (2001)
11. F. Kottmann *et al.*, Hyperf. Interact. **119**, 3 (1999)
12. R. Pohl, Diss. ETH No. 14096, Zürich, 2001
13. T.S. Jensen, V.E. Markushin, Eur. Phys. J. D **21**, DOI: 10.1140/epjd/e2002-00207-y (2002)
14. V.E. Markushin, T.S. Jensen, Proceedings of μCF01, in press
15. T.S. Jensen, V.E. Markushin, πN Newsletter **16**, 358 (2002)
16. T.S. Jensen, V.E. Markushin, Eur. Phys. J. D **19**, 165 (2002)
17. T.S. Jensen, V.E. Markushin, Nucl. Phys. A **689**, 537 (2001)
18. T.S. Jensen, V.E. Markushin, Proceedings of μCF01, in press
19. A.P. Bukhvostov, N.P. Popov, Sov. Phys. JETP **55**, 12 (1982)
20. H.A. Bethe, E.E. Salpeter, *Quantum Mechanics of One- and Two-Electron Atoms* (Academic Press, New York, 1957)
21. T.S. Jensen, V.E. Markushin, PSI-PR-99-32 (1999), nucl-th/0001009
22. T. Koike, Proceedings of μCF01, in press
23. L. Bracci, G. Fiorentini, Nuovo Cim. A **43**, 9 (1978)
24. L.I. Ponomarev, E.A. Solov'ev, JETP Lett. **64**, 135 (1999)
25. L.I. Ponomarev, E.A. Solov'ev, Hyperf. Interact. **119**, 55 (1999)
26. A. Kravtsov, Hyperf. Interact. **119**, 45 (1999)
27. J. Wallenius, P. Froelich, Phys. Rev. A **54**, 1171 (1996)
28. S. Jonsell, J. Wallenius, P. Froelich, Phys. Rev. A **59**, 3440 (1999)
29. G. Bendiscioli *et al.*, Nucl. Phys. A **686**, 317 (2001)

30. J.S. Cohen, Phys. Rev. A **59**, 1160 (1999)
31. G.Ya. Korenman, Hyperf. Interact. **101/102**, 81 (1996)
32. A. Anderhub *et al.*, Phys. Lett. B **71**, 443 (1977)
33. P.O. Egan *et al.*, Phys. Rev. A **23**, 1152 (1981)
34. H. Anderhub *et al.*, Phys. Lett. B **143**, 65 (1984)
35. M. Bregant *et al.*, Phys. Lett. A **241**, 344 (1998)
36. B. Lauss *et al.*, Phys. Rev. Lett. **80**, 3041 (1998)
37. S. Sakamoto *et al.*, Phys. Lett. A **260**, 253 (1999)
38. D. Taqqu *et al.*, Hyperf. Interact. **119**, 311 (1999)
39. F. Kottmann *et al.*, Proceedings of μCF01, in press
40. G. Carboni, G. Fiorentini, Nuovo Cim. B **39**, 281 (1977)
41. R.O. Mueller *et al.*, Phys. Rev. A **11**, 1175 (1975)
42. J.S. Cohen, J.N. Bardsley, Phys. Rev. A **23**, 46 (1981)
43. R. Pohl *et al.*, Proceedings of μCF01, in press
44. R. Pohl, private communication
45. A. Bianconi *et al.*, Phys. Lett. B **487**, 224 (2000)
46. C.A. Baker *et al.*, Nucl. Phys. A **483**, 631 (1988)
47. R. Bacher *et al.*, Z. Phys. A **334**, 93 (1989)
48. K. Heitlinger *et al.*, Z. Phys. A **342**, 359 (1992)
49. C.W.E. Eijk *et al.*, Nucl. Phys. A **486**, 604 (1988)
50. D. Gotta *et al.*, Nucl. Phys. A **660**, 283 (1999)
51. M. Augsburger *et al.*, Nucl. Phys. A **658**, 149 (1999)
52. J. Carbonell, G. Ihle, J.M. Richard, Z. Phys. A **334**, 329 (1989)
53. M.P. Faifman, L.I. Men'shikov, Proceedings of μCF01, in press